Stable Hydrogen Evolution from an AgRhO$_2$ Photocathode Under Visible Light

James Eujin Park[‡], Yuan Hu[‡], Jason W. Krizan, Quinn D. Gibson, Uriel T. Tayvah, Annabella Selloni, Robert J. Cava, and Andrew B. Bocarsly*

Department of Chemistry, Princeton University, Princeton, New Jersey 08544, United States

ABSTRACT: In the search for improved materials for photoelectrochemical water splitting, it has become important to identify new classes of semiconductor materials that may serve as improved photocathodes. To this end, p-type AgRhO$_2$ has been synthesized and tested as a photocathode for water splitting. The AgRhO$_2$ photocathode is found to exhibit excellent photocatalytic capability for reducing protons to H$_2$ across a wide range of pH values with nearly 100% faradaic efficiency and good photostability. Polycrystalline AgRhO$_2$ electrodes exhibit strong preferred c-axis orientation, resulting in anisotropic conductivity, evident from resistivity measurements. AgRhO$_2$ photocathodes are found to provide improved performance and photostability when compared to prior work using a p-CuRhO$_2$ electrode. Enhanced performance is in part attributed to the unusual degree of c-axis orientation found in this material. In addition, there is a significantly lower kinetic barrier for H$_2$ production at the AgRhO$_2$ interface.

Introduction

In the search for novel semiconductor electrodes possessing improved capability for photo-assisted H$_2$ generation, a family of metal oxides crystallizing in the delafossite structure ($A^+B^{3+}O_2$) contains intriguing examples, demonstrating photocatalytic activity not only for H$_2$ generation,[1–7] but also for CO$_2$ reduction.[8–10] A number of papers focusing on synthesizing and characterizing the crystallographic and electrophysical properties of delafossite compounds have been published, including a series of compounds placing Cu, Ag, Pt and Pd on the A site, and different transition metal or rare earth elements on the B site.[11–18] This body of work indicated that delafossites containing Cu or Ag at the A site often produced materials that were intrinsically p-type.[4,8,19–22] When the A site contains a d^{10} monovalent cation, the materials exhibit direct band gaps in the range of 1 to 3.5 eV.[20,23,24]

To date, a limited number of delafossite photocathodes have been reported capable of carrying out photoelectrocatalytic H$_2$ generation, including CuAlO$_2$, CuLaO$_2$, CuCrO$_2$, CuYO$_2$, CuFeO$_2$, and CuRhO$_2$.[1–6] However, these materials are subject to various degrees of photodecompostion.[4,8] The Cu(I) in these lattices is subject to reduction to Cu(0), which degrades the photo-efficiency of the electrode over time.[4,8] In an effort to circumvent this type of photoreductive degradation, previously we reported on p-CuRhO$_2$ which demonstrated a unique self-healing property in the presence of O$_2$ in a basic environment.[4] It was argued that aqueous O$_2$ at high pH is sufficiently oxidizing to suppress Cu(0) formation, thereby keeping the semiconductor surface free of Cu(0) for an extended period.

There has been relatively little research on the photocatalytic evolution of H$_2$ from delafossites containing Ag(I) in the A site. The lack of photocatalytic studies on this material may be due to a common belief that Ag(I) oxide should be more vulnerable to reduction than Cu(I) oxide, since the standard reduction potential for Ag$_2$O is ~700 mV more positive than the standard reduction potential of Cu$_2$O (see Table 1).[25,26] However, this reasoning need not apply to the stability of delafossite materials as the standard reduction potentials will depend on the local environment of Ag(I) and Cu(I). To explore this further, p-type AgRhO$_2$ was synthesized and investigated as a photocathode for photo-assisted H$_2$ generation across a wide range of pH values.

Table 1. The standard reduction potentials ($E°_{red}$) of Cu$_2$O and Ag$_2$O in aqueous solution (pH = 14)[25,26]

| Half-Cell Reaction	$E°_{red}$ vs. SHE
Cu$_2$O + H$_2$O + 2 e$^-$ ↔ 2 Cu + 2 OH$^-$	−0.360 V
Ag$_2$O + H$_2$O + 2 e$^-$ ↔ 2 Ag + 2 OH$^-$	0.342 V

The photocatalytic activity and physical properties of the p-AgRhO$_2$ electrode were compared to its Cu(I) analog, p-CuRhO$_2$ to understand the differences in performance and stability as related to the solid-state properties of the two materials. Although due to cost, AgRhO$_2$ will never be considered a pragmatic material for solar fuel generation, study of this material is of value in developing an understanding of the materials properties that leads to the generation of efficient and stable photocathodes.

Results and Discussion

Synthesis and Structural Properties. Polycrystalline $AgRhO_2$ was synthesized from Ag metal and Rh_2O_3 at 800 °C under an O_2 flow as described in the experimental section. As seen in the SEM image in Figure 1a, the $AgRhO_2$ product adopts a hexagonal habit with a layered morphology. Photoelectrodes were fabricated from pressed pellets, which were prepared by hydrostatic pressing the synthesized $AgRhO_2$ powder at 1 metric ton/0.317 cm^2 area, followed by annealing at 800 °C under an O_2 flow. The pristine electrode surface contains 2D hexagonal flakes with sizes on the order of a few microns (Figure 1b). Figure 1b suggests that when pressed into a pellet, the $AgRhO_2$ powder crystallites stack to yield a strong preferred crystallographic orientation.
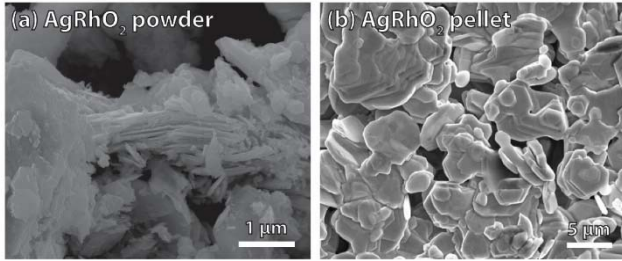
Figure 1. SEM images of (a) synthesized $AgRhO_2$ powder, and (b) a post-annealed $AgRhO_2$ pellet surface. The powder sample exhibits 2D crystallites with a hexagonal habit. When pressed into a pellet, the powder particles stack with strong preferred crystallographic orientation.
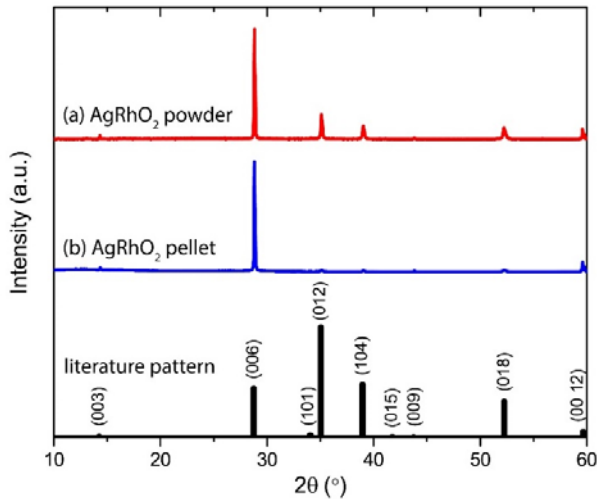

Figure 2. X-ray diffraction (XRD) patterns for (a) synthesized $AgRhO_2$ powder and (b) prepared pressed pellet. The ICSD pattern for $AgRhO_2$ is shown in black.[27] Strong c-axis preferred orientation is observed in the $AgRhO_2$ powder sample, with stronger than theoretically expected intensities for the (003), (006), and (00 12) peaks. This preferential orientation is stronger in the $AgRhO_2$ pellet sample with the (00l) peak intensities even more enhanced.

As observed by x-ray powder diffraction (XRD) pattern (Figure 2), pressed pellets of $AgRhO_2$ yield an unusually strong preferential orientation. Different intensity ratios are observed in both powder and pellet than the reported

literature pattern for $AgRhO_2$ powder which is synthesized by ion exchange from $AgNO_3$ and $LiRhO_2$.[27] The powder pattern shown here exhibits stronger peak intensities for the (003), (006), and (00 12) planes, indicating strong c-axis preferred orientation. The diffraction pattern for the $AgRhO_2$ pellet displays even stronger [001] preferred orientation with peak intensities of the (hk0) peaks much lower compared to the (00l) peaks.

The XRD patterns of $AgRhO_2$ powder and pellet are compared, with the intensity normalized at the (00 12) peak at 59.6° in Figure 3. In this figure, the intensity of the (110) peak at 60.3° is much smaller in the pellet sample than in the powder sample. This difference in preferred orientation between powder and pellet is much less pronounced in analogous powders and pellets of $CuRhO_2$, as also shown in Figure 3. In the XRD patterns for $CuRhO_2$ powder and pellet normalized to their (006) peaks, the intensity of the (110) peak at 60.1° is only approximately half as intense for the pellet as what is observed in the powder.
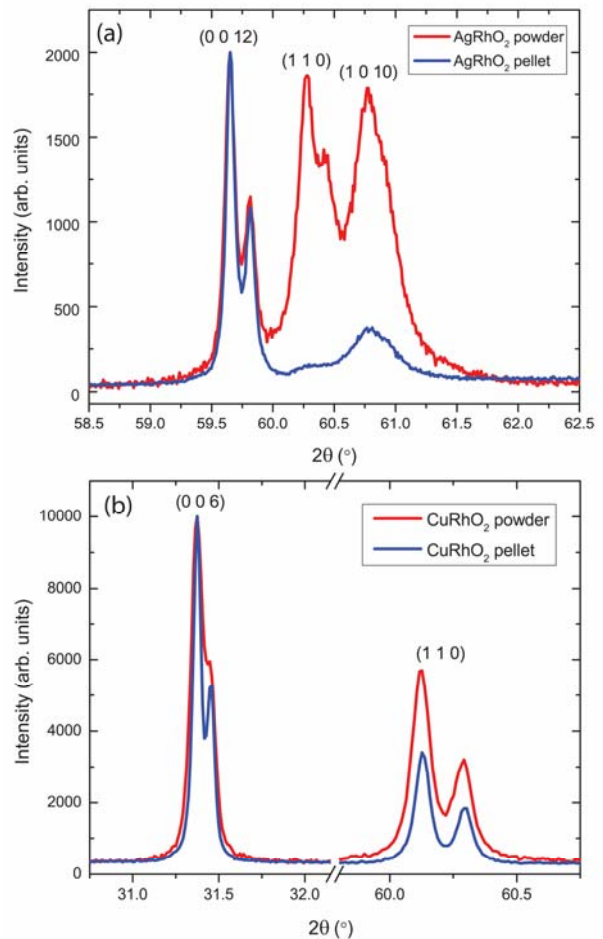

Figure 3. XRD pattern of (a) $AgRhO_2$ and (b) $CuRhO_2$ powder (red) and pellet (blue) with intensity normalized at the (00 12) peak and (006) peak respectively. The peak intensity for (110) in $AgRhO_2$ decreases significantly when pressed into a pellet, indicating stronger c-axis preferred orientation. The (110) peak intensity in $CuRhO_2$, however, decreases to around half when the powder is pressed into pellet, exhibiting weaker c-axis preferred orientation than observed in $AgRhO_2$.

To make the characterization of the preferred orientation more quantitative, preferred orientation parameters for both $AgRhO_2$ powder and pellet were obtained from Rietveld refinement of the XRD patterns shown in Figure 2, utilizing the modified March's function (Figure S1). The Rietveld refinement produced $\chi^2 = 3.39$ and 4.45 for $AgRhO_2$ powder and pellet respectively, indicating acceptable fits. Assuming a uniform distribution of particle orientations ($G_2 = 0$ in the fit function), the $AgRhO_2$ pellet, $G_1 = 0.46$, and powder, $G_1 = 0.83$, both exhibit G_1 values lower than 1. In this function, $G_1 = 1$ indicates that no preferred orientation is present, while $G_1 < 1$ is characteristic of a platy particle habit exhibiting preferred orientation, and $G_1 > 1$ indicates a needle-like particle habit displaying preferred orientation.[28,29] In the current case, the $AgRhO_2$ is seen to display a platy habit, consistent with the micrographs, and the lower G_1 value found for the pellet compared to the powder indicates that the pellet exhibits significantly enhanced preferred orientation of the plates.

The preferred orientation parameters were also obtained for $CuRhO_2$ powder ($G_1 = 0.98 \pm 0.10$) and pellet samples ($G_1 = 0.87 \pm 0.10$) using the same methods. Unlike the $AgRhO_2$ powder, the $CuRhO_2$ powder exhibits almost no preferred orientation with G_1 close to 1. The $CuRhO_2$ pellet shows much weaker preferred orientation ($G_1 = 0.87$) than what was observed in the $AgRhO_2$ pellet ($G_1 = 0.46$). The strong c-axis preferred orientation in the polycrystalline $AgRhO_2$ pellet can result in anisotropic behavior in the physical properties, as is discussed further in a later section of this report.

The pellet density obtained was 85–90% (Table S1) of the theoretical density of single-crystal $AgRhO_2$, suggesting that a highly compacted pellet was obtained. This high density is attributed to the lamellar form of the $AgRhO_2$ particles, which favors oriented packing and minimizes pores between particles. Finally, the as-synthesized $AgRhO_2$ pellet was determined to be p-type using the hot-probe test; a carrier type that has been attributed to the presence of vacancies at the Ag sites, which are hole producing defects.[19,20]

Band Characterization. The band edge positions of $AgRhO_2$ were derived from the band gap energy (E_g), which was determined by the spectral data in Figure 4. Both direct extrapolation (as shown in the figure) and application of the Tauc method provided a band gap of 1.7 eV. Band structure calculations report an indirect lowest energy band gap for $AgRhO_2$.[30] However, Tauc plots were ambiguous in this regard. Plots fit to both a direct and an indirect gap produce a measured band gap of 1.7 eV. The indirect gap Tauc plot is shown in the inset of Figure 4. The valence band edge potential (E_{VB}) was approximated as the flatband potential (E_{FB}) obtained from open-circuit photovoltage measurements as shown in Figure 5 for a typical p-$AgRhO_2$ photocathode. Note that the absorption range of $AgRhO_2$ matches well with the solar spectrum observed on earth. At pH = 0 in a 0.5 M KNO_3 solution, the E_{FB} for p-$AgRhO_2$ was determined to be 0.51 V vs. Ag/AgCl (Figure 5). The E_{FB} values were measured as 0.28 V vs. Ag/AgCl and –0.17 V vs. Ag/AgCl at pH = 5 and 14,
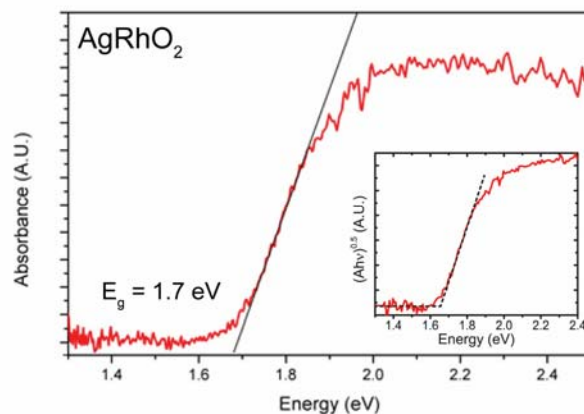
Figure 4. The UV-vis diffuse reflectance spectrum of $AgRhO_2$ (3wt% $AgRhO_2$ in a KBr pellet) showing an absorption onset at 1.7 eV. The spectrum is referenced against a pure KBr pellet. The band gap energy was determined using the Tauc method displayed in the inset for an indirect band gap.
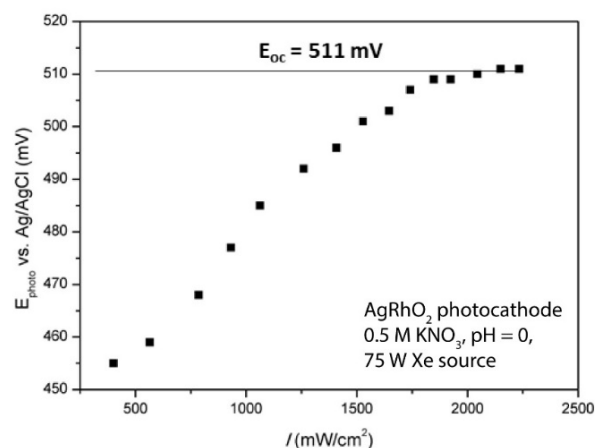
Figure 5. Open-circuit photovoltage measured on $AgRhO_2$ photocathode vs. a Ag/AgCl reference half-cell at pH = 0. The electrode was illuminated with a 75 W focused Xe source, and the intensity of the light at the electrode surface was controlled using crossed polarizing filters. Optical saturation was observed at 0.511 V vs. Ag/AgCl, which was assigned as the flatband potential.

respectively (Figure S2). For a heavily doped p-type semiconductor (majority charge carrier concentration > $10^{18}/cm^3$), the Fermi level is within ~100 mV from the valence band, so E_{FB} can be used as a reasonable approximation for E_{VB}.[31]

The band positions of $AgRhO_2$ vs. Ag/AgCl at different pH values (pH = 0, 5, and 14) derived from the open-circuit photovoltage measurements are depicted in Figure 6. The flatband potential (E_{FB}) of $AgRhO_2$ photocathode shifts negatively by an average of 48 mV/pH from pH = 0 to 14. According to the Nernstian potential for the H_2/H^+ redox couple, this shift should ideally be 59 mV/pH when measured against a pH invariant reference electrode (such as Ag/AgCl). The small deviation from this value suggests that the potential drop across the $AgRhO_2$/aqueous junction is influenced by the chemistry of the Helmholtz layer. It can be assumed that a layer of specifically
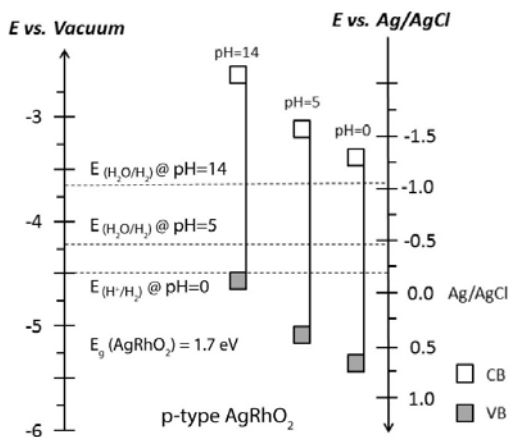
Figure 6. The band edge positions of AgRhO$_2$ at pH = 0, 5, and 14 with respect to the vacuum and Ag/AgCl reference. The valence band edge (E_{VB}) was approximated as the flatband potential (E_{FB}) determined from open-circuit photovoltage measurements. The conduction band edge (E_{CB}) was determined from E_{VB} and band gap energy (E_g = 1.7 eV). The H$_2$O/H$_2$ redox potentials at different pH values are denoted by the dashed lines.

adsorbed protons is present on the oxide surface. Therefore, the Helmholtz layer containing proton and water molecules "buffers" the bulk pH shift at the junction via simple equilibration of water dissociation.[32] This buffer effect may cause the observed E_{FB} shift for the p-type AgRhO$_2$ system to be only 48 mV/pH. A similar pH dependence has been reported for other oxide semiconductors such as n-TiO$_2$ and n-ZnO.[33,34]

Photoelectrochemical Performance. The anticipated photoactivity was confirmed by measuring the incident photon-to-current conversion efficiency (IPCE) for p-AgRhO$_2$ photoelectrodes (Figure 7). A three-electrode cell
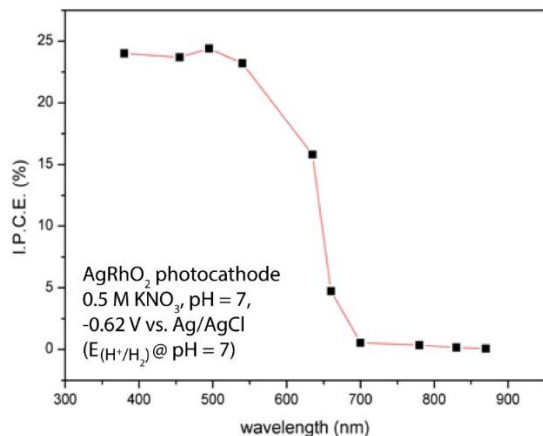
Figure 7. Incident photon-to-current conversion efficiency (IPCE) plot collected under illumination at various photon wavelengths held at the reduction potential of H$_2$ (−0.62 V vs. Ag/AgCl) in 0.5 M KNO$_3$ solution adjusted to pH = 7. The photocurrent rapidly increases at ~700 nm, saturating around 550 nm at an ICPE of 25%. The observed photoactivity is in agreement with the band gap energy (E_g = 1.7 eV) measured in the UV-vis diffuse reflectance spectrum.

(Ag/AgCl as the reference electrode) in 0.5 M KNO$_3$ aqueous electrolyte at pH = 7 was utilized with the electrode held at the H$_2$ reduction potential (−0.62 V vs. Ag/AgCl). A rapid onset in the photocurrent was observed at ~700 nm which saturated around 550 nm at an IPCE of 25%.

The photocurrent-potential plots (*I–V* characteristics) of a p-AgRhO$_2$ photocathode were collected using a conventional three-electrode configuration, with Ag/AgCl as the reference and a Pt mesh as the counter electrode, in a 0.5 M KNO$_3$ aqueous electrolyte. The light source was a 465 nm LED with an output of 15 mW/cm^2. An effective photo response in both acidic (pH = 0) and basic (pH = 14) solutions was observed in the *I–V* characteristics under chopped illumination (Figure 8). Increased cathodic photocurrent as the potential is swept into the negative direction confirms the p-type nature of the AgRhO$_2$ photocathode.
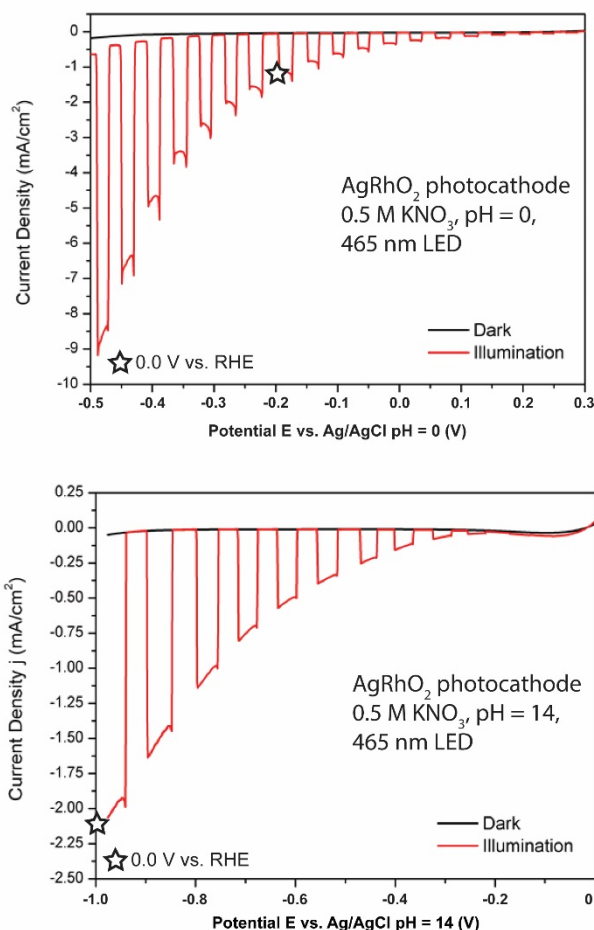
Figure 8. The linear sweep voltammograms on a p-AgRhO$_2$ photocathode in 0.5 M KNO$_3$ solution adjusted to pH = 0 (top) and 14 (bottom) with photocurrents under chopped 465 nm illumination (red) and dark current (black). The star represents 0.0 V vs. RHE. In both acidic and basic conditions, photocurrent is observed with little dark current. The photocurrent increases on negative sweep of the potential, consistent with the p-type nature of the AgRhO$_2$ photocathode.
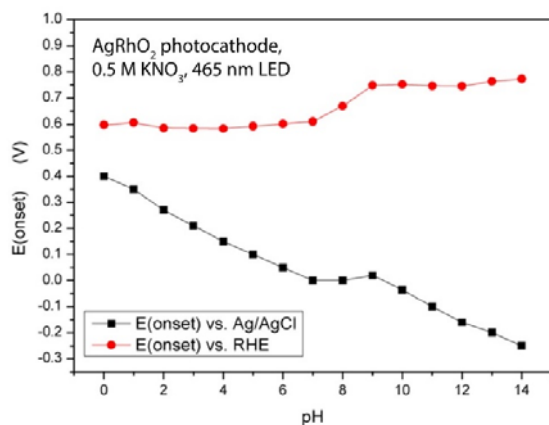
Figure 9. The photocurrent onset potentials (E_{onset}) of a p-AgRhO$_2$ photocathode at various pH conditions and plotted with respect to RHE (red dots) and Ag/AgCl (black squares) reference electrodes. Overall Nernstian response is observed with the overall 60 mV shift per pH unit. However, the irregularity seen at pH ~8 is hypothesized to be due to the deprotonation of the surface.

The photocurrent onset potential (E_{onset}) observed as a function of pH is plotted with respect to both Ag/AgCl and RHE in Figure 9. In this figure, a shift in E_{onset} is observed as a function of pH. The RHE trace given in Figure 9 removes the pH effect of the electrolyte. In this presentation, E_{onset} is seen to have a consistent value of ~0.6 V vs. RHE from pH = 0 to 7 and ~0.8 V vs. RHE from pH = 9 to 14. We attribute the overall 60 mV per pH unit shift to the expected Nernstian response of the system.[10,35] The increased slope of the onset shift in basic electrolyte is assigned to the inner Helmholtz layer, which is affected by the surface chemical properties.[32] We hypothesize that the electrode surface has pK$_a$ ~8 and that the deprotonation of the surface modifies the pH response of the interface for pH values greater than pH ~7. This assignment of the surface pK$_a$ is consistent with reports on other metal oxide electrode systems.[36–38]

From the *I–V* characteristics, the E_{onset} at pH = 0, 5, and 14 are in good agreement with the flatband potentials (E_{FB}) determined from the open-circuit photovoltage measurement. At pH = 0, the flatband potential is 0.51 V vs. Ag/AgCl, while the photocurrent onset potential is ~0.4 V vs. Ag/AgCl. The offset of ~100 mV between E_{onset} and E_{FB}, also observed at pH = 5 and 14, might be due to a small kinetic barrier, however, this difference is mainly accounted for by experimental error. Thus, the interfacial kinetic barrier is modest for the reduction of H$^+$ and H$_2$O on p-AgRhO$_2$. Our previous report on the analogous p-type CuRhO$_2$ photocathodes indicated that the difference between E_{onset} and E_{FB} was ~800 mV for H$_2$ production in that system.[4] We suggest that this difference in overpotential between AgRhO$_2$ and CuRhO$_2$ is a major reason for the AgRhO$_2$ system being more stable than the CuRhO$_2$ system, as discussed further below.

The photocatalytic activity of the p-type AgRhO$_2$ photocathode was further analyzed with quantitative bulk electrolyses at zero bias with respect to E_{redox} of H$_2$O/H$_2$ at the selected pH values (pH = 0, pH = 7, and pH = 14) with 465 nm LED (Figure 10). In the absence of illumination, independent of pH, no current was observed and H$_2$

production ceased. A linear correlation between the H$_2$ generation and the photocurrent was observed in the electrolyses independent of pH for ~7 hrs, the longest time period tested in this study. During this time, photocurrent was stable and little dark current was observed. The faradaic efficiency and quantum yield for each pH condition shown in Figure 10 are summarized in Table 2. Consistent with the observed photocurrent stability we find that the faradaic efficiency for H$_2$ formation is 100% within our measuring error and invariant over the observation period. The quantum yield of ~10% suggests fast electron–hole recombination. We suspect this is due to the polycrystalline nature of our electrodes which provides for surface recombination at grain boundaries and surface defects.[39]
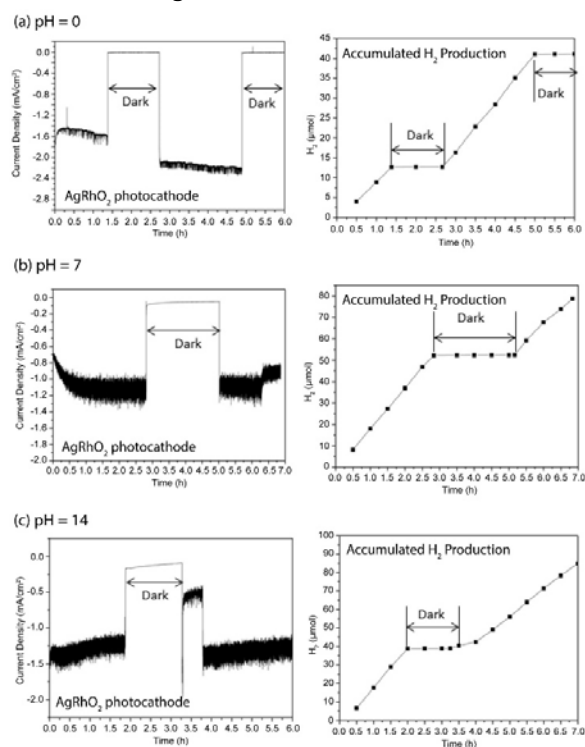
Figure 10. The J_{photo}–time profiles of AgRhO$_2$ photocathode under potentiostatic condition at zero bias with respect to the H$_2$O/H$_2$ redox potential (left) and the accumulated H$_2$ concentration along with the electrolysis process (right), at (a) pH = 0, (b) pH = 7, and (c) pH = 14. In this pH range, steady H$_2$ production is observed under illumination with faradaic efficiency for H$_2$ production 100% within our measuring error. In the absence of illumination, the H$_2$ production ceased. The step in photocurrent for pH = 14 at 3.5 h is due to the H$_2$ bubbles building up on the electrode surface.

Table 2. Tabulated faradic efficiency and quantum yield at 465 nm for H$_2$ evolution at p-type AgRhO$_2$ as a function of pH

pH	0	7	14
Faradaic Efficiency	94.3 ± 4.7 %	95.2 ± 4.8 %	96.5 ± 4.8 %
Quantum Yield	6.1 ± 0.6 %	9.9 ± 0.1 %	10.8 ± 0.1 %

Photostability. Unlike our previous report on p-type CuRhO$_2$ photocathodes,[4] where the gradual build-up of

elemental Cu on the electrode surface in a non-oxidative environment was observed, p-type AgRhO$_2$ displays good stability in a non-oxidative environment, as well as stability across a wide range of pH. The stable performance of the p-AgRhO$_2$ photocathode is directly related to the lack of autoreduction at the silver sites under illumination. This finding is based on several spectroscopic analyses of the AgRhO$_2$ electrode surface after extended electrolysis. SEM images collected on the AgRhO$_2$ pellets after electrolysis (for 6 h) at various pH values (Figure S3) reveal pristine surfaces with no apparent change in surface morphology. In contrast to our results on CuRhO$_2$, where the XRD patterns showed the presence of Cu(0) after electrolysis, the XRD patterns on the post-electrolysis electrode surfaces of AgRhO$_2$ do not yield diffraction features indicative of Ag(0) (Figure S4).[4]

The Ag to Rh to O ratios in the post-electrolysis samples by EDS (in Table 3) remained unchanged when compared to the Ag:Rh:O ratio of 1:1:2 for the pristine material, supporting the conclusion that the system is chemically stable under illumination. Again, this is in contrast to our studies of CuRhO$_2$ electrode, where photodegradation led to the Cu:Rh ratio changing from 1:1 to 1.7:1 under non-oxidative conditions, which was attributed to an accumulated metallic Cu on the surface.

Table 3. Energy dispersive spectroscopy (EDS) elemental analysis on the atomic percentage of Ag, Rh and O collected from a pristine sample of AgRhO$_2$ and samples after electrolyses performed under different pH conditions.

Element at. % (± 5%)	Pristine	pH = 0	pH = 7	pH =14
Ag	22	25	19	23
Rh	23	26	19	24
O	55	49	62	53
Ag:Rh:O (±5%)	1:1:2	1:1:2	1:1:2	1:1:2

Since both XRD and EDS probe a material's bulk properties, x-ray photoelectron spectroscopy (XPS) was employed to specifically assess surface degradation. XPS spectra of AgRhO$_2$ collected on a pristine sample and post electrolysis samples at pH = 0, 7, and 14 (Figure S5) showed that the primary Ag(I) signals at $3d_{5/2}$ = 368.07 eV and $3d_{3/2}$ = 374.07 eV remained unchanged.[40–42] However, due to the *ex situ* nature of our XPS measurements, any Ag metal generated on the surface of our electrode is expected to be oxidized by air exposure during the transfer of our samples from the electrolysis cell to the XPS. Therefore, the atomic percentage of Ag and Rh from the XPS data was compared; since, reduction of the surface to zero valent Ag should form at least a partial Ag overlayer that would modify the XPS observed Ag:Rh ratio. We find the pristine surface consists of 36at% Ag and 64at% Rh. On a post-electrolysis sample at pH = 7, the atomic percentage (at%) of Ag and Rh were found to be 35at% and 65at%. Therefore, within the error of our measurements, the photoreduction of Ag(I) on the

AgRhO$_2$ surface does not occur, in contrast to the behavior observed in the CuRhO$_2$ system.

The observed enhanced photostability of p-AgRhO$_2$ can in part be associated with the highly preferred orientation of polycrystalline AgRhO$_2$ pellets which exposes a very high percentage of [001] crystal faces as shown in Figure 2. In a previous report by Rodgers *et al.*, an anisotropy in the conductivity was observed on various single crystal delafossite materials including CuFeO$_2$ and AgFeO$_2$, a set of systems that provides an analogy with the two systems under consideration here.[12] In that work, it was shown that the resistivity is around three orders of magnitude higher when measured along the *c*-axis than perpendicular to the *c*-axis (i.e. in the plane of the layers).

To evaluate our system, the direction-dependent resistivity was measured at 300 K on a polycrystalline AgRhO$_2$ pellet using a four point probe. The resistivity in the pellet plane, dominated by the (00*l*) planes orientation of particles, was measured as 38.5 ± 7.0 Ω cm. However, when measured perpendicular to the plane of the pellet, which is dominated by the *c*-axis of the particles, the resistivity was 180 ± 54 Ω cm, around five times higher. This anisotropic behavior in resistivity directly pertains to the electrodes of interest, since the measurements were conducted on a polycrystalline sample that was formed in an identical manner to the electrodes. We assume that a much larger anisotropic behavior occurs in a single crystal sample. The resistivity for the CuRhO$_2$ pellet, which exhibits less preferred orientation, was measured to be 46.3 ± 0.1 Ω cm. The carrier conductivities in the plane of the electrode surface are similar for both AgRhO$_2$ and CuRhO$_2$ on the exposed surface.
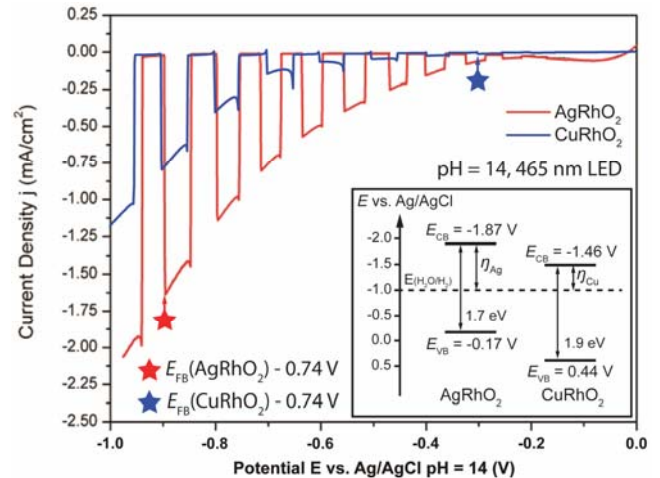
Figure 11. The linear sweep voltammograms on p-AgRhO$_2$ (red) and p-CuRhO$_2$ (blue) at pH = 14 under chopped 465 nm illumination. The inset displays the band structures at pH = 14. CuRhO$_2$ has a large kinetic barrier for H$_2$ generation based on the large difference between E_{onset} and E_{FB} of ~800 mV, while this is only ~100 mV for AgRhO$_2$. In order to compare the photocatalytic activity of the two materials, the red star and blue star show the potentials where the two materials have the same degree of band bending (0.74 V). Note that under this condition, AgRhO$_2$ generates two orders of magnitude higher photocurrent than CuRhO$_2$.

To compare the photocatalytic activity of p-AgRhO$_2$ and p-CuRhO$_2$ photocathodes, the I–V characteristics under chopped 465 nm illumination were collected on for both electrodes under the same electrochemical conditions at pH = 14 (Figure 11). This pH was selected to optimize the stability and photocurrent response of the CuRhO$_2$ system. It is immediately obvious that the photocurrent response of the AgRhO$_2$ system is superior when the electrodes are compared at the same potential. However, a more pertinent comparison is the observed photocurrent under conditions of constant band bending for the two systems. The inset in Figure 11 shows that the conduction band edges for copper and silver rhodate (as approximated open-circuit photopotential data) are displaced by ~400 mV, with AgRhO$_2$ having the more negative band edge.[4] Thus, at constant potentials of comparison the band bending in these two systems is quite different.

We have arbitarily selected 740 mV of band bending in Figure 11 as shown by the star symbols. Under this band bending condition, the photocurrent is two orders of magnitude larger for AgRhO$_2$. For any level of band bending (greater than ~100 mV), one anticipates that AgRhO$_2$ will generate more photocurrent than CuRhO$_2$ due to the "built in overpotential" of the interface. That is, given the positions of the conduction band edges of these two materials, the silver system supplies photogenerated electrons that are 870 mV beyond the water redox potential, while the photogenerated electrons in the copper system are only 460 mV beyond this potential (Figure 11 inset). Based on this difference in overpotential, a larger current is expect for the silver system than the copper system.

However, it is easy to see that there is a second factor coming into play. Namely, one doesn't observe any significant photocurrent from CuRhO$_2$ until the potential is ~700 mV beyond the flatband potential, while in the AgRhO$_2$ system, photocurrent is easily observed once 100 mV of band bending is achieved. Further, in neither system is the photocurrent maximized at 1 V of band bending, which is well beyond the band bending needed to efficiently separate charge at an ideal interface. Thus, there must be a kinetic limitation in these systems which is not associated with a difference in the "built in overpotential", and this kinetic limitation requires large band bending to drive the reaction at a reasonable rate. This kinetic bottleneck to interfacial charge transfer is much more significant at the CuRhO$_2$ surface than at the AgRhO$_2$ interface.

Whether, the enhancement in proton reduction on the AgRhO$_2$ interface is a function of anisotropic conductivity or is related to the chemical composition of the electrode surface is a question that will take further study. We do note that the strong preferential orientation of AgRhO$_2$ polycrystalline samples, a phenomena that is not observed for with CuRhO$_2$, also exposes more basal plane to the electrolyte (over edge plane) and this may be a source of the low kinetic barrier for H$_2$ generation.

Based on the XRD pattern of the AgRhO$_2$ pellet, the (00l) [l = 3, 6, 9, 12…] planes are preferentially exposed on the surface. The structure of AgRhO$_2$ comprises layers of edge-shared octahedra (RhO$_6$) stacked between Ag(I) ions that are linearly coordinated to oxygen atoms.[27] The (00l) planes correspond to either the Ag plane or the RhO$_6$ layer. Based
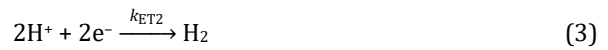
on the XPS data presented, it is likely that the RhO$_6$ layer is present at the semiconductor-electrolyte interface, as higher atomic percentage of Rh over Ag is detected on the surface. This suggests the RhO$_6$ layer is the catalytic interface for H$_2$ generation. This conclusion is furthur supported by our previous work on CuRhO$_2$ and CuFeO$_2$ where we only observe H$_2$ generation in the presence of CO$_2$ from the CuRhO$_2$ surface.[4,8] However, we observed CO$_2$ reduction when CuFeO$_2$ is the photocathode,[8] suggesting the FeO$_6$ layer is less catalytic for H$_2$ generation than the RhO$_6$ layer. For AgRhO$_2$ which preferentially exposes more RhO$_6$ layers due to the c-axis preferred orienation, the photocatalytic activity for H$_2$ generation is improved compared to its analogue, CuRhO$_2$.

The difference in stability between AgRhO$_2$ and CuRhO$_2$ can be explained in terms of different rates of charge transfer kinetics. Upon illumination, the possible reactions for the photoinduced electron are:

For AgRhO$_2$,

$$2H^+ + 2e^- \xrightarrow{k_{ET1}} H_2 \tag{1}$$

$$Ag^+ + e^- \xrightarrow{k_{Ag}} Ag^0 \tag{2}$$

For CuRhO$_2$,

$$2H^+ + 2e^- \xrightarrow{k_{ET2}} H_2 \tag{3}$$

$$Cu^+ + e^- \xrightarrow{k_{Cu}} Cu^0 \tag{4}$$

The interfacial charge transfer reactions (1) and (3) result in the production of hydrogen with rate constants, k_{ET1} for AgRhO$_2$ and k_{ET2} for CuRhO$_2$. Based on the different offsets between E_{onset} and E_{FB}, k_{ET1} is larger than k_{ET2}. However, the photoinduced electron can also chemically perturb the electrode surface by the reduction of Ag(I) to Ag(0) for AgRhO$_2$ (2) and Cu(I) to Cu(0) for CuRhO$_2$ (4) with rate constants, k_{Ag} and k_{Cu} respectively. For AgRhO$_2$, which has a relatively low kinetic barrier for H$_2$ production, surface photoreduction is not observed as Ag(0) is not detected on the surface after electrolysis. This implies that the rate constant for interfacial charge transfer (k_{ET1}) is much higher than the rate constant for photoreduction of Ag$^+$ (k_{Ag}). On the other hand, the surface of CuRhO$_2$, which has a large kinetic barrier for H$_2$ production, suffers from reductive photocorrosion with Cu(0) detected on the surface after electrolysis.[4] In this case, k_{ET2} must be smaller than k_{Cu}. We conclude that the difference in photostability between AgRhO$_2$ and CuRhO$_2$ can be attributed to these relative differences in rate constants for the reduction of protons versus the reduction of the coinage metal cation siting in the delafossite A-site.

Conclusions

Our novel p-type AgRhO$_2$ photocathode, which has the same crystal structure as previously reported for CuRhO$_2$, was studied for the photo-assisted reduction of protons and water to H$_2$. AgRhO$_2$ demonstrated good photostability across a wide range of pH values with a nearly unit faradaic efficiency. Strong preferred orientation along the c-axis was observed and resulted in an anisotropic resistivity, which is

approximiately five times higher along the *c*-axis than in the plane perpendicular to the *c*-axis. The fabricated electrode surface exhibits lower resistivity similar to cathodes composed of $CuRhO_2$. The difference in photocatalytic activity and photostability between $AgRhO_2$ and $CuRhO_2$ is attributed to the different rate of interfacial charge transfer versus photocorrosion for the Ag^+ and Cu^+ systems; the p-$AgRhO_2$ electrode exhibiting a higher rate for interfacial charge transfer than the rate for photocorrsion, and vice versa for p-$CuRhO_2$.

Experimental Section

Materials. The $AgRhO_2$ powder sample was prepared via the ceramic method from a mixture of stoichiometric Ag powder (Strem Chemical, 99.9%) and Rh_2O_3 powder (Strem Chemical, 99.9%). The Rh_2O_3 powder was dried at 700 °C in air overnight. Both of the starting materials were analyzed by x-ray diffraction (XRD) on a Bruker D8 Advance Eco X-ray diffractometer using Cu Kα radiation (0.154 nm).

The Ag and Rh_2O_3 powders were ground in an agate mortar and transferred to an alumina crucible. The reaction mixture was heated in a Lindberg/Blue tube furnace at 800 °C (ramp rate: 3 °C/min) for 12 hours under flowing O_2 (Airgas). The temperature was then lowered to 500 °C (ramp rate: 3 °C/min), and the sample was then quenched to room temperature. This process was repeated after thoroughly regrinding the sample with subsequently monitoring the reaction progress by powder XRD.

The $CuRhO_2$ powder samples were prepared as reported in our previous work by reacting a stoichiometric amount of CuO (99.7%, Alfa Aesar) and Rh_2O_3 at 850 °C under a mixed gas atmosphere (O_2 : Ar = 1:99 by volume).[4] The $CuRhO_2$ powder samples were then pressed into 6.35 mm (*ca.* 1 mm thick) pellets with a hydraulic pressure press at 1 metric ton/0.317 cm^2 area, followed by annealing at 850 °C under the same mixed gas atmosphere or at 1100 °C under air, followed by reacting at 850 °C under the mixed gas atmosphere.[4]

Electrode Fabrication. The $AgRhO_2$ powder was pressed into 6.35 mm (*ca.* 1 mm thick) and 3.18 mm (*ca.* 3 mm thick) pellets using a hydraulic pressure press at 1 metric ton/0.317 cm^2 area and at 1/4 metric ton/0.0794 cm^2 area respectively. This was followed by densifying at 800 °C under O_2 flow for 12 hours. The polycrystalline pellet was then attached to a copper lead using conductive silver adhesive (Epoxy Technology E3037), followed by a thermal cure at 150 °C for approximately 2 hours. The silver adhesive also served as an effective ohmic contact between the semiconducting $AgRhO_2$ and the metallic copper wire. The current-potential (*I–V*) characteristic collected across a pellet connected to the copper lead on both sides by conductive silver adhesive demonstrated a linear relationship, achieving ohmic contact at the semiconductor/metal junction (Figure S6). The as-assembled semiconductor was installed into a glass tube with a bent tip holding the pellet end. The gap between the glass and the pellet was sealed by epoxy (LOCTITE 0151™ Epoxi-Patch® Adhesive) for water-proofing.

Characterization. The band gap of $AgRhO_2$ was determined by diffuse reflectance spectroscopy on a UV-vis spectroscopy (HP 8453 UV-visible spectroscopy system) equipped with an integrating sphere (Labsphere RSA-HP-8453 Reflectance Spectroscopy Accessory). The diffuse reflectance spectrum was collected on a KBr pellet consisting of 3wt% $AgRhO_2$, using a pure KBr pellet as the blank. The band gap energy of $AgRhO_2$ was found as the intersection with the abscissa by extrapolating the absorption edge in the spectrum.[43,44] The Tauc method was also used to confirm the band gap energy.

The electrical conductivity type of $AgRhO_2$ was determined to be p-type by a hot-probe Seebeck coefficient test. The positive terminal and negative terminal of an ammeter were wired to the two ends of a $AgRhO_2$ pellet, and then a heated soldering iron was put into close contact with the pellet surface connected to the negative terminal. The majority charge carriers were determined to be holes as the ammeter indicated a positive current flow.

Four point probe resistivity was measured using a Quantum Design physical property measurement system (PPMS) Dynacool. $AgRhO_2$ and $CuRhO_2$ pellets were cut into rectangles (approximately 3.0 mm by 1.0 mm, 0.4 mm thickness), and platinum wires were attached to the samples with Ag paint. The resistivity was measured at 300 K with a constant current of 0.5 mA through the sample.

The XRD patterns were collected with Bruker D8 Advance Eco diffractometer equipped with Cu Kα (λ = 1.5418 Å) and a Lynxeye detector. The preferred orientation parameters were obtained through Rietveld refinement using the Fullprof Program Suite. The SEM images and EDX analysis were collected on an FEI Quanta 200 FEG Environmental-SEM and Oxford Instruments INCA EDX system. The oxidation states of the electrode surface components were investigated by X-ray photoelectron spectroscopy (XPS) on an ESCA station (VG Scientific LTD.) equipped with a Mg anode (Mg Kα = 1253.6 eV). The C 1s peak for aliphatic hydrocarbons with a binding energy of 284.6 eV was employed as an internal reference for peak position correction.

Electrochemical Measurement. The photoelectrochemical measurements were conducted using a CH Instrument Electrochemical Analyzer 1140 potentiostat-galvanostat. A typical three-electrode setup was employed for the photoelectrochemcial cell (PEC), consisting of a $AgRhO_2$ working electrode, a Pt mesh counter electrode and a Ag/AgCl reference electrode. 0.5 M KNO_3 (Fisher Scientific, 99.9%) aqueous solution was used as the supporting electrolyte solution, with the solution pH value being adjusted to different levels using diluted HNO_3 (aq.) or 1 M KOH solution (aq.). The supporting electrolyte was deaerated by purging Ar gas for an extended time.

The light sources employed for the photoelectrochemical measurements were either a 75 W PTI Xenon arc lamp (USHIO UXL 151H) equipped with band filters, or monochromatic light emitting diodes (LED, Cree) equipped with an optical lens. The open-circuit photovoltage (E_{oc}) of $AgRhO_2$ was measured with a voltmeter with varying incident light intensity with respect to a Ag/AgCl reference. The incident photon-to-current conversion efficiency (IPCE) was determined by Equation (5) with LED illuminations at various wavelengths.

$$[IPCE\%] = \frac{1240 \times j_{photo}(\mu A \cdot cm^{-2})}{\lambda \, (nm) \times P \, (W/m^{-2})} \times 100\% \qquad (5)$$

In this equation, j_{photo} is the photocurrent density, λ is the illumination wavelength, and P is the intensity of the incident light source as measured at the electrode surface. The photocurrent density (j_{photo}) was calculated as the difference of the dark current density and photocurrent density. The monochromatic photon flux was measured at each wavelength using a calibrated Si photodiode (Fieldmaster 33-0506, Coherent Inc.), placed at an equivalent distance from the light source to the electrode, and corrected by accounting the absorbance of the aqueous solution and the Pyrex cell® according to previous report.[4]

Photo-assisted H_2 generation at an $AgRhO_2$ photoelectrode was performed under potentiostatic conditions in a gas-tight cell under constant illumination and stirring with a modified PEC configuration previously reported in detail.[45] The counter electrode was housed in a gas dispersion tube (Ace glass, porosity 4–8 μm). For an extended experiment, the evolved gas from the cathodic chamber was collected by the water displacement method. Gaseous product was quantitated by gas chromatography on a Hewlett-Packard G1530A equipped with a TCD detector.

ASSOCIATED CONTENT

Supporting Information
The Supporting Information is available free of charge on the ACS Publications website at DOI:
Rietveld refinement of $AgRhO_2$ XRD patterns, dimensions and density of pellets, additional open-circuit photovoltage measurements, SEM images and XRD patterns of electrode surface, XPS spectra, current–voltage curve across pellet.

AUTHOR INFORMATION

Corresponding Author
* E-mail: bocarsly@princeton.edu

Author Contributions
‡J.E.P. and Y.H. contributed equally.

Notes
The authors declare no competing financial interest.

ACKNOWLEDGMENT

REFERENCES

(1) Koriche, N.; Bouguelia, A.; Aider, A.; Trari, M. Photocatalytic Hydrogen Evolution over Delafossite $CuAlO_2$. *Int. J. Hydrog. Energy* **2005**, *30*, 693–699.

(2) Younsi, M.; Aider, A.; Bouguelia, A.; Trari, M. Visible Light-Induced Hydrogen over $CuFeO_2$ via $S_2O_3^{2-}$ Oxidation. *Sol. Energy* **2005**, *78*, 574–580.

(3) Trari, M.; Bouguelia, A.; Bessekhouad, Y. P-Type $CuYO_2$ as Hydrogen Photocathode. *Sol. Energy Mater. Sol. Cells* **2006**, *90*, 190–202.

(4) Gu, J.; Yan, Y.; Krizan, J. W.; Gibson, Q. D.; Detweiler, Z. M.; Cava, R. J.; Bocarsly, A. B. P-Type $CuRhO_2$ as a Self-Healing Photoelectrode for Water Reduction under Visible Light. *J. Am. Chem. Soc.* **2014**, *136*, 830–833.

(5) Saadi, S.; Bouguelia, A.; Derbal, A.; Trari, M. Hydrogen Photoproduction over New Catalyst $CuLaO_2$. *J. Photochem. Photobiol. Chem.* **2007**, *187*, 97–104.

(6) Saadi, S.; Bouguelia, A.; Trari, M. Photocatalytic Hydrogen Evolution over $CuCrO_2$. *Sol. Energy* **2006**, *80*, 272–280.

(7) Kang, D.; Kim, T. W.; Kubota, S. R.; Cardiel, A. C.; Cha, H. G.; Choi, K.-S. Electrochemical Synthesis of Photoelectrodes and Catalysts for Use in Solar Water Splitting. *Chem. Rev.* **2015**, *115*, 12839–12887.

(8) Gu, J.; Wuttig, A.; Krizan, J. W.; Hu, Y.; Detweiler, Z. M.; Cava, R. J.; Bocarsly, A. B. Mg-Doped $CuFeO_2$ Photocathodes for Photoelectrochemical Reduction of Carbon Dioxide. *J. Phys. Chem. C* **2013**, *117*, 12415–12422.

(9) Wuttig, A.; Krizan, J. W.; Gu, J.; Frick, J. J.; Cava, R. J.; Bocarsly, A. B. The Effect of Mg-Doping and Cu Nonstoichiometry on the Photoelectrochemical Response of $CuFeO_2$. *J. Mater. Chem. A* **2016**, *5*, 165–171.

(10) White, J. L.; Baruch, M. F.; Pander, J. E.; Hu, Y.; Fortmeyer, I. C.; Park, J. E.; Zhang, T.; Liao, K.; Gu, J.; Yan, Y.; et al. Light-Driven Heterogeneous Reduction of Carbon Dioxide: Photocatalysts and Photoelectrodes. *Chem. Rev.* **2015**, *115*, 12888–12935.

(11) Prewitt, C. T.; Shannon, R. D.; Rogers, D. B. Chemistry of Noble Metal Oxides. II. Crystal Structures of $PtCoO_2$, $PdCoO_2$, $CuFeO_2$, and $AgFeO_2$. *Inorg. Chem.* **1971**, *10*, 719–723.

(12) Shannon, R. D.; Rogers, D. B.; Prewitt, C. T.; Gillson, J. L. Chemistry of Noble Metal Oxides. III. Electrical Transport Properties and Crystal Chemistry of ABO_2 Compounds with the Delafossite Structure. *Inorg. Chem.* **1971**, *10*, 723–727.

(13) Shannon, R. D.; Rogers, D. B.; Prewitt, C. T. Chemistry of Noble Metal Oxides. I. Syntheses and Properties of ABO_2 Delafossite Compounds. *Inorg. Chem.* **1971**, *10*, 713–718.

(14) Benko, F. A.; Koffyberg, F. P. Optical Interband Transitions Of The Semiconductor $CuGaO_2$. *Phys. Status Solidi Appl. Res.* **1986**, *94*, 231–234.

(15) Benko, F. A.; Koffyberg, F. P. Opto-Electronic Properties of p- and n-Type Delafossite, $CuFeO_2$. *J. Phys. Chem. Solids* **1987**, *48*, 431–434.

(16) Benko, F. A.; Koffyberg, F. P. Opto-Electronic Properties of $CuAlO_2$. *J. Phys. Chem. Solids* **1984**, *45*, 57–59.

(17) Benko, F. A.; Koffyberg, F. P. Preparation and Opto-Electronic Properties of Semiconducting $CuCrO_2$. *Mater. Res. Bull.* **1986**, *21*, 753–757.

(18) Sheets, W. C.; Mugnier, E.; Barnabé, A.; Marks, T. J.; Poeppelmeier, K. R. Hydrothermal Synthesis of Delafossite-Type Oxides. *Chem. Mater.* **2006**, *18*, 7–20.

(19) Marquardt, M. A.; Ashmore, N. A.; Cann, D. P. Crystal Chemistry and Electrical Properties of the Delafossite Structure. *Thin Solid Films* **2006**, *496*, 146–156.

(20) Nagarajan, R.; Duan, N.; Jayaraj, M. K.; Li, J.; Vanaja, K. A.; Yokochi, A.; Draeseke, A.; Tate, J.; Sleight, A. W. P-Type Conductivity in the Delafossite Structure. *Int. J. Inorg. Mater.* **2001**, *3*, 265–270.

(21) Snure, M.; Tiwari, A. $CuBO_2$: A p-Type Transparent Oxide. *Appl. Phys. Lett.* **2007**, *91*, 092123.

(22) Kawazoe, H.; Yasukawa, M.; Hyodo, H.; Kurita, M.; Yanagi, H.; Hosono, H. P-Type Electrical Conduction in Transparent Thin Films of $CuAlO_2$. *Nature* **1997**, *389*, 939–942.

(23) Sheets, W. C.; Stampler, E. S.; Bertoni, M. I.; Sasaki, M.; Marks, T. J.; Mason, T. O.; Poeppelmeier, K. R. Silver Delafossite Oxides. *Inorg. Chem.* **2008**, *47*, 2696–2705.

(24) Yanagi, H.; Kawazoe, H.; Kudo, A.; Yasukawa, M.; Hosono, H. Chemical Design and Thin Film Preparation of P-Type Conductive Transparent Oxides. *J. Electroceramics* **2000**, *4*, 407–414.

(25) Bard, A. J.; Parsons, R.; Jordan, J. *Standard Potentials in Aqueous Solution*; CRC Press, 1985.

(26) Bratsch, S. G. Standard Electrode Potentials and Temperature Coefficients in Water at 298.15 K. *J. Phys. Chem. Ref. Data* **1989**, *18*, 1–21.

(27) Todorova, V.; Leineweber, A.; Kienle, L.; Duppel, V.; Jansen, M. On $AgRhO_2$, and the New Quaternary Delafossites $AgLi_{1/3}M_{2/3}O_2$, Syntheses and Analyses of Real Structures. *J. Solid State Chem.* **2011**, *184*, 1112–1119.

(28) Dollase, W. A. Correction of Intensities for Preferred Orientation in Powder Diffractometry: Application of the March Model. *J. Appl. Crystallogr.* **1986**, *19*, 267–272.

(29) Joseph, S.; Kamath, P. V.; Upadhya, S. Electrochemical Synthesis of Oriented CuO Coatings on Stainless Steel Substrates: Solution-Mediated Control over Orientation. *J. Electrochem. Soc.* **2009**, *156*, E18–E22.

(30) Jain, A.; Ong, S. P.; Hautier, G.; Chen, W.; Richards, W. D.; Dacek, S.; Cholia, S.; Gunter, D.; Skinner, D.; Ceder, G.; et al. Commentary: The Materials Project: A Materials Genome Approach to Accelerating Materials Innovation. *APL Mater.* **2013**, *1*, 011002.

(31) Memming, R.; Schwandt, G. Potential and Charge Distribution at Semiconductor-Electrolyte Interfaces. *Angew. Chem. Int. Ed. Engl.* **1967**, *6*, 851–861.

(32) Gerischer, H. Neglected Problems in the pH Dependence of the Flatband Potential of Semiconducting Oxides and Semiconductors Covered with Oxide Layers. *Electrochimica Acta* **1989**, *34*, 1005–1009.

(33) Bolts, J. M.; Wrighton, M. S. Correlation of Photocurrent-Voltage Curves with Flat-Band Potential for Stable Photoelectrodes for the Photoelectrolysis of Water. *J. Phys. Chem.* **1976**, *80*, 2641–2645.

(34) Butler, M. A.; Ginley, D. S. Prediction of Flatband Potentials at Semiconductor-Electrolyte Interfaces from Atomic Electronegativities. *J. Electrochem. Soc.* **1978**, *125*, 228–232.

(35) Johansson, E.; Boettcher, S. W.; O'Leary, L. E.; Poletayev, A. D.; Maldonado, S.; Brunschwig, B. S.; Lewis, N. S. Control of the pH-Dependence of the Band Edges of Si(111) Surfaces Using Mixed Methyl/Allyl Monolayers. *J. Phys. Chem. C* **2011**, *115*, 8594–8601.

(36) Shimizu, K.; Lasia, A.; Boily, J.-F. Electrochemical Impedance Study of the Hematite/Water Interface. *Langmuir* **2012**, *28*, 7914–7920.

(37) Qu, F.; Morais, P. C. The pH Dependence of the Surface Charge Density in Oxide-Based Semiconductor Nanoparticles Immersed in Aqueous Solution. *IEEE Trans. Magn.* **2001**, *37*, 2654–2656.

(38) Kosmulski, M. The pH-Dependent Surface Charging and the Points of Zero Charge. *J. Colloid Interface Sci.* **2002**, *253*, 77–87.

(39) Ghosh, A. K.; Fishman, C.; Feng, T. Theory of the Electrical and Photovoltaic Properties of Polycrystalline Silicon. *J. Appl. Phys.* **1980**, *51*, 446–454.

(40) Hoflund, G. B.; Hazos, Z. F.; Salaita, G. N. Surface Characterization Study of Ag, AgO, and Ag_2O Using x-Ray Photoelectron Spectroscopy and Electron Energy-Loss Spectroscopy. *Phys. Rev. B* **2000**, *62*, 11126–11133.

(41) Weaver, J. F.; Hoflund, G. B. Surface Characterization Study of the Thermal Decomposition of AgO. *J. Phys. Chem.* **1994**, *98*, 8519–8524.

(42) Hoflund, G. B.; Weaver, J. F.; Epling, W. S. Ag_2O XPS Spectra. *Surf. Sci. Spectra* **1994**, *3*, 157–162.

(43) Kubelka, P.; Munk, F. An Article on Optics of Paint Layers. *Z Tech Phys* **1931**, *12*, 593–601.

(44) Murphy, A. B. Band-Gap Determination from Diffuse Reflectance Measurements of Semiconductor Films, and Application to Photoelectrochemical Water-Splitting. *Sol. Energy Mater. Sol. Cells* **2007**, *91*, 1326–1337.

(45) Baruch, M. F.; Pander, J. E.; White, J. L.; Bocarsly, A. B. Mechanistic Insights into the Reduction of CO_2 on Tin Electrodes Using in Situ ATR-IR Spectroscopy. *ACS Catal.* **2015**, *5*, 3148–3156.

Authors are required to submit a graphic entry for the Table of Contents (TOC) that, in conjunction with the manuscript title, should give the reader a representative idea of one of the following: A key structure, reaction, equation, concept, or theorem, etc., that is discussed in the manuscript. Consult the journal's Instructions for Authors for TOC graphic specifications.

Insert Table of Contents artwork here